W. Assmus [a], C. Gross [a], A. Muiznieks [b], G. Raming [b], A. Mühlbauer [b], C. Stenzel [c]

a) Physikalisches Institut, Johann Wolfgang Goethe-Universität, Frankfurt am Main, Germany
b) Institut für Elektrowärme, Universität Hannover, Germany
c) Dornier GmbH, Friedrichshafen, Germany

Power consumption of Skull melting

1. Introduction

Inductive Skull melting of oxides (and other materials with comparable electrical conductivity) is based on direct inductive heating of an electrically conducting melt by an alternating electromagnetic (RF) field. Heating is thereby accomplished by ohmic losses caused by eddy currents induced in the melt; materials with very high melting temperature (3000 K and above) can be molten by this method [1]. The melt is typically contained in a cold crucible with a palisade-like wall consisting of water-cooled copper tubes. During a Skull run, a thin layer of non-molten material remains on the inside of the crucible wall (the so-called 'Skull'), which prevents direct contact of the melt with the crucible material; Skull melting is therefore often said to be 'quasi-crucible-free'. For this reason, Skull melting is especially advantageous for crystal growth of materials, for which conventional crucibles (metal or ceramic material with direct melt contact) are inadequate, because they cannot withstand the required temperature or lead to contamination of the melt with crucible materials.

As typical for direct inductive heating methods, the required electrical power strongly depends on the chosen working frequency, which must be adjusted to the electrical conductivity of the melt and the size of the crucible. The electromagnetic field is not only absorbed in the melt, but also in the inductor coil and the crucible, which are usually made of copper. These ohmic losses can be considerable at an unfavourably chosen frequency and can indirectly prevent a successful Skull run, in view of limited output power of the RF generator.

As a consequence of the principle, Skull melting is intrinsically linked with a heatflow from the melt through the crust to the crucible, where the heat is being removed by the cooling water. In addition, heat losses can occur due to radiation, especially for melts in crucibles with large diameter. In order to obtain an overall power balance, these losses must be replaced by an equivalent energy absorption in the melt. Important experimental

quantities as, e.g., the achievable melt volume for a given RF input power are being determined by this power balance.

Basic properties of this power balance have been discussed in detail by SEKERKA et al for a melt process closely related to Skull melting, the so-called 'internal centrifugal zone growth' (ICZG). We apply parts of the theoretical background outlined by SEKERKA to Skull melting and extend the analytical model by a quantitative description of the losses occurring in the inductor coil and the crucible. In the experimental section, we check our analytical results by comparison with calorimetric data obtained from real Skull runs. We use a melt consisting of ZrO_2 with Y_2O_3 addition, since we have extensive experience in crystallizing this material, which is used as a diamond gemstone replacement [8].

As will be shown, a good agreement between analytical and experimental data can be observed. On the other hand, some of the assumptions made in section 2 in order to simplify the analytical model seem to be rather crude. Therefore the work presented here has been accompanied by: 1) numerical calculations (finite element method) of axisymmetric coupled electromagnetic and temperature fields in the sample [7] and 2) numerical calculations (boundary element method) of 3D RF electromagnetic field in the cold crucible [6]. Experimental and analytical data presented in this paper are compared with results obtained from these calculations in section 4.

2. Analytical calculations

2.1. Power balance in the Skull melting process

To start with, it is helpful to deal with the absorbed electromagnetic power in the melt (P_{me}) and the thermal power removed from the melt (P_{th}) separately, although these quantities are not independent (must equal each other) in an equilibrium situation. Fig. 1 shows a schematic diagram of P_{me} and P_{th} as a function of the melt radius r_{me} for different fixed inductor currents $I_1 < I_2 < I_3 < I_4$ and frequencies. (The curves are presented here without axis units and are interpreted qualitatively only, but are in fact calculated from the expressions derived in the following sections.) For most values of r_{me} , P_{me} differs from P_{th} , and in an experiment, r_{me} will increase or decrease in order to reduce the imbalance. For a sufficiently high inductor current (i.e. increased power input to the melt), both curves will intersect in two points. Point (A) in Fig. 1 corresponds to a stable equilibrium of the melt radius r_{me} , since the increase in P_{th} is bigger than the increase in P_{me} for a slightly larger r_{me}, and vice versa for a slightly smaller r_{me}. As a consequence, the system is stabilizing itself at a fixed melt radius. Point (B) corresponds to an instable equilibrium and is not discussed here in more detail, since the

corresponding experimental situation is unlikely to occur in pure form during Skull melting, because it is obscured by the start-up process, which is required to initiate Skull melting [1]. The described self-stabilizing effect occurs for all melt radii $r_{me} \geq r_B$ (shaded area in Fig. 1). The width of the stable region depends on the frequency and typically decreases for lower frequency (see Fig. 1 right). The latter statement is confirmed by numerical investigation of the stability of the molten zone [7].

In the following sections, expressions for the different losses will be derived and the electromagnetic efficiencies of coil, crucible and melt will be calculated. In the framework of the analytical calculations performed here, inductor coil, crucible and melt are considered to be of infinite length along their symmetry axis (thus the inhomogeneity of the fields in axial direction is neglected); related to a finite length, we get finite values for the absorbed power again.

2.2. Thermal losses

For the determination of thermal losses of the melt, we restrict ourselves here to losses by heat conduction through the Skull crust and neglect losses by radiation. This assumption appears acceptable in view of the high aspect-ratio (height:diameter) of the crucible used in the experiments. According to the last paragraph, we consider radial heat flow only and thermal losses are given by:

$$P_{th} = \frac{2\,\pi\,\lambda_{sc}\,h_{me}\,(T_{me} - T_{cw})}{\ln(r_{cr}/r_{me})} \qquad (1)$$

where λ_{sc} is the effective heat conductivity of the crust (other symbols see Tab. 1 and Fig. 6). If all other parameters are known from experiment, eq. 1 may be used to determine λ_{sc} (see section 4), which is difficult to measure by other methods in the temperature range relevant here.

2.3. Absorbed electromagnetic power

For the determination of the absorbed power in coil (P_{co}), crucible (P_{cr}) and melt (P_{me}), the electrical equivalent circuit of the Skull system depicted in Fig. 2 was used. Since we are interested in ohmic losses here, it includes non-reactive parts only. The additional resistances R_{me} and R_{cr} in the coil circuit appear due to the presence of the crucible and the melt inside the coil. From $P = R\,(I_{co})^2$, we get the corresponding losses P_{co}, P_{cr} and P_{me}.

2.3.1. Coil losses

In the frequency range considered here (100 kHz - 10 MHz), the skin effect is fully developed in all copper parts, and the ohmic losses in these parts can be calculated to a good approximation by assuming a skin layer of finite depth δ (skin depth) with a constant current density inside this layer and no current at all in the depth of the material. From this model (see Fig. 3), we get:

$$R_{co} = \frac{\rho_{co}\, l_{co}}{\pi\, d_{ct}\, \delta_{co}} \tag{2}$$

2.3.2. Crucible losses

The currents in the cooling fingers of the crucible are induced by the RF field of the inductor coil. In accordance with our main approximation (section 2.1., last paragraph), we assume that these currents are restricted to the parts of the cooling fingers, which are situated inside the coil. This assumption seems reasonable, if we look at the current density calculated by numerical simulation (see Fig. 4, for details see [6]), where the induced currents are indeed restricted essentially to the range inside the coil. From a simple argument (the currents in the cooling fingers must screen their inside from the magnetic field of the coil, which is related to the coil current I_{co}), we obtain

$$R_{cr} = n_{co}^{\,2}\, \frac{\pi\, d_{cf}\, \rho_{cr}\, n_{cf}}{h_{co}\, \delta_{cr}} \tag{3}$$

2.3.3. Absorption in the melt

In contrast to the skin depth in the copper parts (δ_{co}, δ_{cr}), the skin depth in the melt (δ_{me}) may be comparable in size to the radius of the melt, depending on the resistivity of the melt (ρ_{me}) and the frequency (f). The approximation made in sections 2.3.1 and 2.3.2 is therefore not valid here, and we derive an expression for R_{me} from the general solution of the underlying field equation in the 'infinitely long' cylindrical geometry [3]:

$$R_{me} = n_{co}^{\,2}\, \frac{\pi\, \omega\, \mu\, r_{me}^{\,2}}{h_{co}}\, \frac{h_{me}}{h_{co}}\, 2\, \Re\left(E_d(r_{me})\right) \tag{4}$$

where the dimensionless electric field E_d is given by

$$E_d(r) = - \frac{1-i}{2} \frac{\delta_{me}}{r_{me}} \frac{J_1(k\,r)}{J_0(k\,r_{me})} \qquad (5)$$

(with $\Re(z)$: real part of z , $k = (1\text{-}i) / \delta_{me}$: complex wave number and $J_n(z)$: Bessel function of first kind, n-th order). To simplify matters, we assumed an electrically isolating Skull crust and a temperature-independent resistivity of the melt. This approximation is reasonable at least for ionic conductors as oxides, which are known to have a steep decrease of resistivity with increasing temperature up to the melting point (i.e. the cold Skull crust has a much higher resistance compared to the melt) and a more or less constant resistivity above T_m . The correction factor h_{me} / h_{co} in eq. 4 takes into account that the height of the melt is typically smaller than the height of the coil.

The resistivity of the melt (ρ_{me}) enters into eq. 4 via $\delta_{me} = \sqrt{\rho_{me} / \pi \mu f}$ and k. If interpreted as a function of ρ_{me} only (all other parameters fixed), eq. 4 is non-monotonous, i.e. the inverse of eq. 4 with respect to ρ_{me} is a multi-valued function. This means that ρ_{me} can not be determined unambiguously from eq. 4 only, even if all other parameters are known from the experiment. For this purpose one has to use a different measurement scheme (measurement of the complex impedance of the Skull system) or ρ_{me} must be deduced from a set of several experiments with varying parameters.

The power absorbed in coil, crucible and melt is shown in Fig. 5 (left) for a set of realistic parameters (see tab 1). Starting with an experimental value for $P_{th} = P_{me}$ (5060 W), eq. 4 & 5 were used to determine the coil current $I_{co} = \sqrt{P_{me} / R_{me}}$ for a given frequency. Subsequently, the coil and crucible losses were calculated using eq. 2 & 3.

2.3.4. Electromagnetic efficiency

The electromagnetic efficiencies of the coil (η_{co}), the crucible (η_{cr}) and the melt (η_{me}) are defined here in the following manner:

$$\eta_{co} = \frac{R_{co}}{R_{to}} = \frac{P_{co}}{P_{to}} , \quad \eta_{cr} = \frac{R_{cr}}{R_{to}} = \frac{P_{cr}}{P_{to}} , \quad \eta_{me} = \frac{R_{me}}{R_{to}} = \frac{P_{me}}{P_{to}} \qquad (6)$$

where $$R_{to} = R_{co} + R_{cr} + R_{me} , \quad P_{to} = P_{co} + P_{cr} + P_{me} \qquad (7)$$

These quantities are shown in Fig. 5 (right) as a function of frequency f ; all other parameters have been chosen according to the experiment (see tab 1).

3. Experiment

Experiments have been carried out with a vacuum tube generator ($P_{RF,max}$ = 25 kW) operating at a working frequency of 3.82 MHz. A cross-sectional view of the Skull crucible used in this work is given in Fig. 6, the dimensions are listed in Tab 1. Losses in the different parts of the Skull system have been determined calorimetrically by measuring flow and temperature difference in separate cooling water circuits (see Fig. 7). Water flow is measured by turbine flow meters and varies between ≈ 5 *l*/min (inductor coil) and 30 *l*/min (crucible). Water temperature is measured by resistive temperature sensors (Pt100, direct diving type), with temperature differences between water inlet and outlet of about 1 - 2 K. Losses are calculated from the following formula:

$$P_{cal} = \Phi \rho_o c_o \Delta T \qquad (8)$$

with measured water flow Φ [m³/s], density of water ρ_o = 1000 kg/m³ , specific heat capacity of water c_o = 4190 J/(kg K) and the measured temperature difference ΔT.

In the cooling water circuit of the crucible, two different contributions show up: the power absorbed in the crucible due to its ohmic losses (P_{cr}) and the power absorbed in the melt and led to the crucible via conduction (P_{me}). These two contributions can be separated with the help of the coil current I_{co} (which is continuously monitored during Skull runs) and a separate experiment with an *empty* crucible (where obviously P_{me} = 0). The measurement error of the calorimetric set-up is estimated to be ± 50 W.

The Skull crucible (see Fig. 4, dimensions see tab 1) was filled with approx. 1 kg of ZrO_2 powder with 12 mol% Y_2O_3 addition; Zr metal pellets were used for start-up. After oxidizing the metal and establishing a molten zone, the input power was held constant for several hours during which the calorimetric measurement was performed. After cooling down, the ingot was cut in two halves and the melt radius (r_{me}) and melt height (h_{me}) were measured.

4. Results and discussion

Using experimental results and eq. 1, we get λ_{sc} = 3.37 W/mK. This value is comparable to the heat conductivity of dense ceramic zirconia (3 - 5 W/mK). Since eq. 1 assumes radial heat flow only, this result should be interpreted as an upper estimate for the 'true' thermal conductivity of the crust, which is expected to fall in the interval of the thermal conductivity of zirconia fibre board (0.1 - 0.5 W/mK) and ceramic zirconia. The calculated value is therefore very reasonable.

The resistivity of the melt can not be calculated unambiguously from the experiment described here, as explained in section 2.3.3. Using eq. 4, we get $\rho_{me} = 0.72 \cdot 10^{-3}$ Ωm *or* $\rho_{me} = 2.50 \cdot 10^{-3}$ Ωm ; both values are of the same order of magnitude and compare well to data reported in literature ($0.3 - 1.0 \cdot 10^{-3}$ Ωm, [2, 5]).

As can be seen in Fig. 5, the losses in coil and crucible are small (≈ 6%) and nearly constant for frequencies higher than a critical frequency, which can be characterised by a skin depth comparable to $r_{me}/2$. For lower frequencies, the coil current I_{co} must be increased (by increasing the RF input power) in order to maintain the necessary power absorption in the melt, which is required to stabilize a given melt volume. This increased coil current leads in turn to much higher losses in the copper parts, which eventually dominate the overall power consumption at about one tenth of the critical frequency or below. These losses may prevent successful Skull melting, in view of limited output power of the RF generator. Therefore, the working frequency should be chosen to be equal or higher than the critical frequency, as defined above.

Experimental, analytical and numerical results agree well in general (see tab. 2). A closer look at the results reveals that both analytical and numerical calculation underestimate the power absorbed in the copper parts. This may be explained in part by the proximity effect (concentration of the current in the coil on the inner side) or contact resistances at the terminals of the coil, which have not been taken into account.

To sum up, we have developed an analytical model for Skull melting, which describes the power absorption in the coil, crucible and melt. We have shown by comparison with experimental and numerical data, that the analytical model provides realistic values for the absorbed power, despite some simplifying assumptions. We could determine the thermal conductivity of the Skull crust from experimental results, which is difficult to measure by other methods and is an important input parameter for numerical simulations. Future work should check the validity of the analytical model on a broader experimental basis, e.g. by use of different crucibles and materials.

5. Acknowledgements

Financial support was granted by the European Space Research and Technology Centre (ESTEC) under subcontract (DO 14 10 159 I 00 367). The authors would like to thank K.-D. Luther for his continuous help with the laboratory work.

This paper is a modified version of a two-part article which appeared in *Cryst. Res. Technol.* [4, 7].

6. References

[1] V.I. ALEKSANDROV in 'Current Topics in Materials Science', ed. E. Kaldis, North Holland (1978), pp 421

[2] R.E.W. CASSELTON, Proc. British Ceramic Soc. 10 (1971) 265

[3] E.J. DAVIES, Conduction and induction heating, (Peregrinus, London, 1990)

[4] C. GROSS, Cryst. Res. Technol. (Power consumption of Skull melting, Part I), Vol. 34 (1999), No. 3, 319-328

[5] L. HEYNE, Proc. British Ceramic Soc. 19 (1971) 229

[6] A. MÜHLBAUER, "Electrohydrodynamic Analysis", ESTEC Studies and Developments Related to Microgravity Environment Utilisation (WO10), Noordwijk, The Netherlands, 10 / 98

[7] A. MUIZNIEKS, Cryst. Res. Technol. (Power consumption of Skull melting, Part II), Vol. 34 (1999), No. 3, 329-338

[8] K. NASSAU, Lapidary Journal Vol 31 (1977), 900

[9] R.F. SEKERKA, J. Crystal Growth 50 (1980), 783-800

Figure and table captions

Fig 1: Absorbed electromagnetic power in the melt (P_{me}) and thermal power removed from the melt (P_{th}) as a function of the melt radius r_{me} for different inductor currents $I_1 < I_2 < I_3 < I_4$ and frequencies (schematic). Point *A*: stable equilibrium, Point *B*: instable equilibrium. The little arrows between the curves illustrate the stabilizing / destabilizing effect for a small deviation from the equilibrium points. The shaded area marks the stable region in the high frequency case (left, inductor current I_2) and the low frequency case (right, inductor current I_4).

Fig 2: Electrical equivalent circuit of the Skull system. The additional resistances R_{cr} and R_{me} in the coil circuit appear due to the presence of the crucible and the melt inside the coil.

Fig 3: The skin layer in the cooling fingers of the crucible (***left***) and the inductor coil tube (***right***) with current direction (*I*). The 'true' current density distrubition is approximated by assuming a distinct skin layer with a constant current density (see text).

Fig 4: One half of the Skull crucible (dimensions see Tab. 1). ***A***: Palisade-like crucible wall (water-cooled copper tubes), ***B***: Isolines of the induced surface current (taken from numerical calculation, ref. [6]), ***C***: Inductor coil, ***D***: Crucible bottom (with slit in order to minimise electromagnetic screening).

Fig 5: Absorbed power in coil, crucible and melt for Skull melting of ZrO_2, curves calculated from analytical model, parameters see tab 1. ***left***: absolute values (with constant power in the melt, P_{th} = 5060W), ***right***: as a percentage of total absorbed power (efficiencies). The vertical dotted line denotes the frequency, where 2 $\delta_{me} = r_{me}$.

Fig 6: Cross-sectional view of the Skull crucible used in this work (schematic). *A*: Melt volume, ***B***: sintered crust, ***C***: Palisade-like crucible wall (water-cooled copper tubes), ***D***: inductor coil, ***E***: crucible bottom, ***F***: compacted powder. The symbols used for the dimensions (e.g. h_{cr}, h_{co}) are explained in Tab 1, where numeric values are given also.

Fig 7: Experimental set-up for calorimetric measurements in the cooling water circuits (schematic). *F1..4*: turbine flow meters, *T1..5*: temperature sensors (Pt100).

Tab 1: Used symbols and parameter values.

Tab 2: Absorbed power in coil, crucible and melt: Comparison between experimental, analytical and numerical results, parameters see Tab. 1, P_{to} : total absorbed power, ***l.c.p.***: losses in copper parts (coil and crucible) related to P_{to} , *: without and with current lead of the coil.

Tab 1: Used symbols and parameter values.

h_{me}	height of melt	34	mm
r_{me}	radius of melt	17	mm
r_{cr}	inner radius of crucible	25	mm
h_{cr}	height of crucible (inside)	150	mm
n_{cf}	number of cooling fingers	18	-
d_{cf}	diameter of cooling fingers	10	mm
n_{co}	coil windings	5	-
d_{ct}	diameter of coil tube	6	mm
d_{ci}	inner diameter of coil	90	mm
h_{co}	height of coil	54	mm
l_{co}	length of coil tube (= $n_{co}\,\pi(d_{cf}+d_{ci})$)	1508	mm
ρ_{co}	spec. elec. res. of coil (Cu @ RT)	1.7e-8	Ωm
ρ_{cr}	spec. elec. res. of crucible (Cu @ RT)	1.7e-8	Ωm
ρ_{me}	spec. elec. res. of melt (ZrO_2 @ T_m)	1.0e-3	Ωm
λ_{sc}	thermal conductivity of Skull crust	1,5	W/mK
T_{me}	melt temperature (here: $T_m(ZrO_2)$)	2750	°C
T_{cw}	temperature of cooling water	40	°C
I_{co}	inductor coil current (RMS)	44,2	A
f	working.frequency	3,82	MHz

Tab 2: Absorbed power in coil, crucible and melt: Comparison between experimental, analytical and numerical results, parameters see Tab. 1, P_{to} : total absorbed power, ***l.c.p.***: losses in copper parts (coil and crucible) related to P_{to} , *: without and with current lead of the coil.

	exp.	analyt.	num.
P_{me} [W]	5060	5657	6000
P_{cr} [W]	380	265	234
P_{co} [W]	340	81 / 119 *	110
P_{to} [W]	5780	6041	6344
l.c.p. [%]	12	6	5

Fig 1: Absorbed electromagnetic power in the melt (P_{me}) and thermal power removed from the melt (P_{th}) as a function of the melt radius r_{me} for different inductor currents $I_1 < I_2 < I_3 < I_4$ and frequencies (schematic). Point *A*: stable equilibrium, Point *B*: instable equilibrium. The little arrows between the curves illustrate the stabilizing / destabilizing effect for a small deviation from the equilibrium points. The shaded area marks the stable region in the high frequency case (left, inductor current I_2) and the low frequency case (right, inductor current I_4).

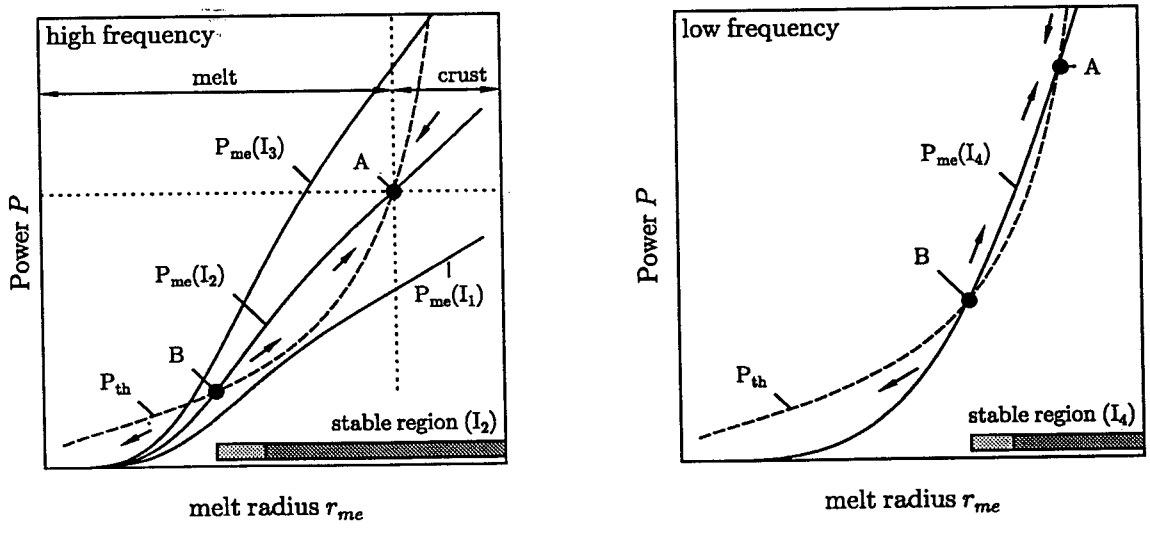

Fig 2: Electrical equivalent circuit of the Skull system. The additional resistances R_{cr} and R_{me} in the coil circuit appear due to the presence of the crucible and the melt inside the coil.

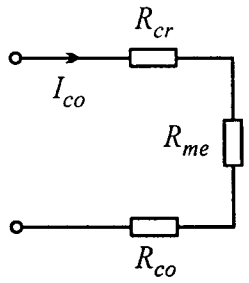

Fig 3: The skin layer in the cooling fingers of the crucible (***left***) and the inductor coil tube (***right***) with current direction (I). The 'true' current density distrubition is approximated by assuming a distinct skin layer with a constant current density (see text).

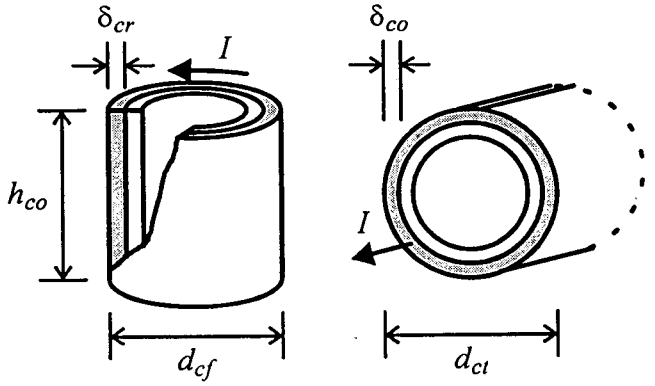

Fig 4: One half of the Skull crucible (dimensions see Tab. 1). ***A***: Palisade-like crucible wall (water-cooled copper tubes), ***B***: Isolines of the induced surface current (taken from numerical calculation [6]), ***C***: Inductor coil, ***D***: Crucible bottom (with slit in order to minimise electromagnetic screening).

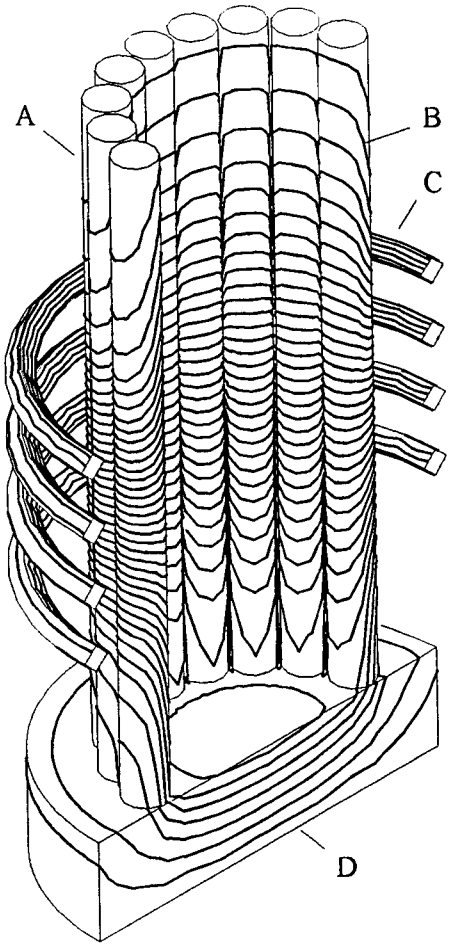

Fig 5: Absorbed power in coil, crucible and melt for Skull melting of ZrO_2, curves calculated from analytical model, parameters see tab 1. ***left***: absolute values (with constant power in the melt, P_{th} = 5060W), ***right***: as a percentage of total absorbed power (efficiencies). The vertical dotted line denotes the frequency, where 2 $\delta_{me} \doteq r_{me}$.

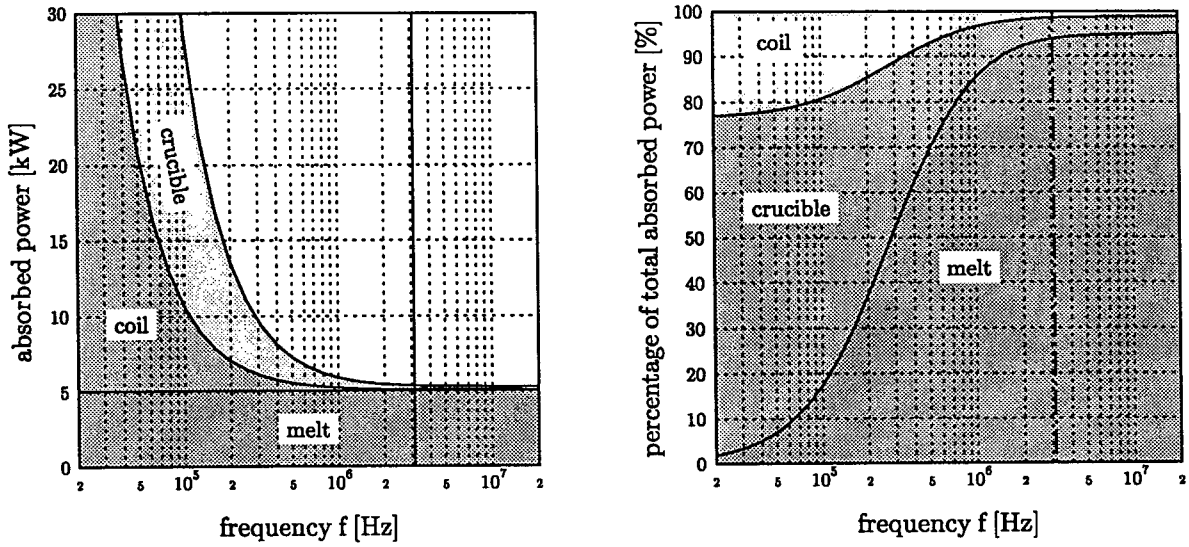

Fig 6: Cross-sectional view of the Skull crucible used in this work (schematic). ***A***: Melt volume, ***B***: sintered crust, ***C***: Palisade-like crucible wall (water-cooled copper tubes), ***D***: inductor coil, ***E***: crucible bottom, ***F***: compacted powder. The symbols used for the dimensions (e.g. h_{cr}, h_{co}) are explained in Tab 1, where numeric values are given also.

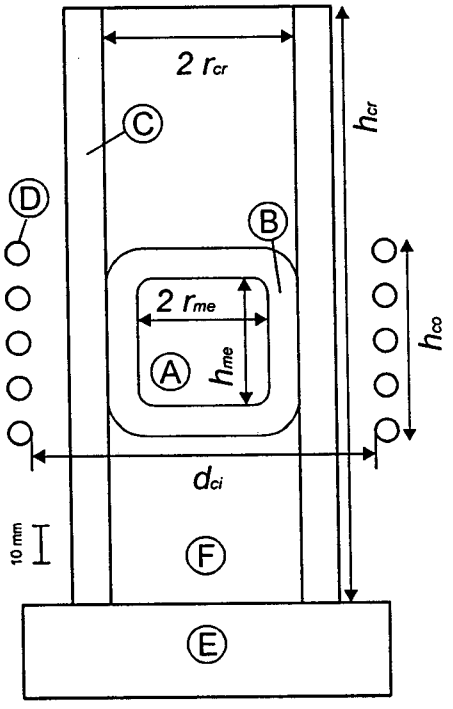

Fig 7: Experimental set-up for calorimetric measurements in the cooling water circuits (schematic). *F1..4*: turbine flow meters, *T1..5*: temperature sensors (Pt100).

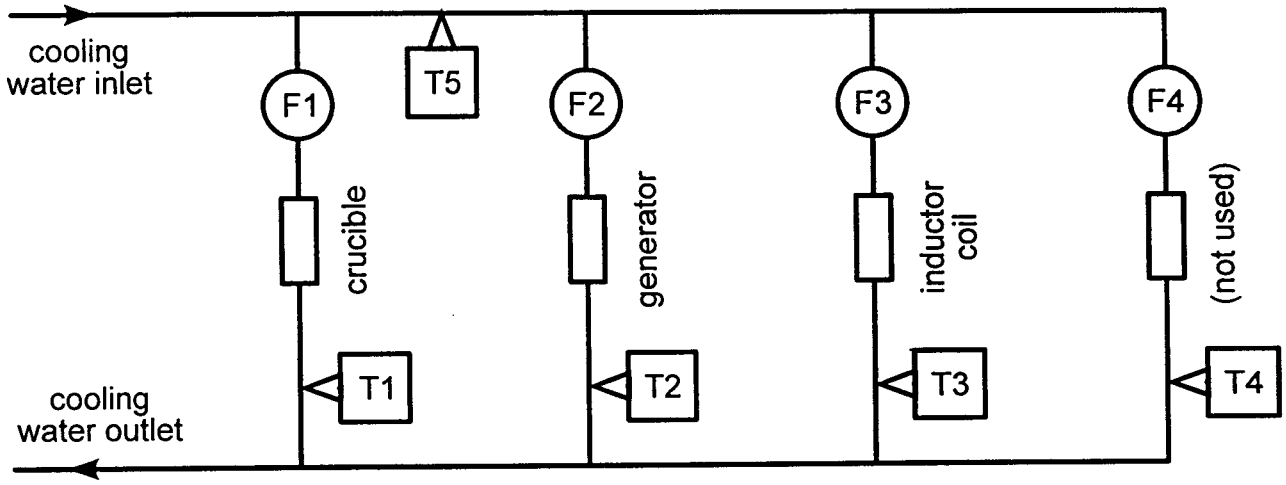

Authors' addresses:

Prof. Dr. Wolf Assmus (corresponding)
Dr. C. Gross
Physikalisches Institut
Johann Wolfgang Goethe-Universität
Robert-Mayer-Str. 2-4
D-60054 Frankfurt am Main
Germany

e-mail: assmus@physik.uni-frankfurt.de
Tel.: +49 / 69 / 798 - 23144
Fax.: +49 / 69 / 798 - 28520

Dr. Andris Muiznieks
Georg Raming
Prof. Dr. A. Mühlbauer
Institut für Elektrowärme
Universität Hannover
Wilhelm-Busch-Str. 4
D-30167 Hannover
Germany

Dr. Christian Stenzel
Dornier GmbH
Abt. RIO 41
D-88039 Friedrichshafen
Germany

running title:

ASSMUS et al.: Power consumption of Skull melting